DOI 10.24425/aee.2026.1525

Distance-dependent detection reliability of fixed-threshold residual earth-fault indicators in medium-voltage feeders

Ines Bula Bunjaku[1], Avni Alidemaj[2]✉, Drenusha Gashi[3], Donjeta Latifi[4], Edin Bula[5]

[1]*Department of Computing and Information Technologies, RIT Kosovo (A.U.K.)*
Prishtina, Kosovo

[2]*Department of Energy Engineering, UBT – Higher Education Institution*
Prishtina, Kosovo

[3]*Kosovo Electricity Distribution Company (KEDS)*
Prishtina, Kosovo

[4]*Market Operations Engineer, KOSTT Sh.A.*
Prishtina, Kosovo

[5]*CEO, E&I Mechatronic*
Prishtina, Kosovo

e-mail: ibula@auk.org, ✉ avni.alidemaj@ubt-uni.net, {drenushagashi14/edinbula2}@gmail.com, donjeta.latifi@kostt.com

(Received: 11.03.2026; revised: 17.08.2026)

Abstract: Residual earth-fault indicators installed in medium-voltage overhead feeders operate with fixed pickup thresholds, while the available residual current decreases with feeder distance. As a result, indicator operation becomes progressively less reliable toward remote feeder sections, and deterministic short-circuit analysis alone is insufficient to characterize practical detectability limits. This study investigates distance-dependent detectability of fixed-threshold residual earth-fault indicators using a combined experimental, simulation-based, and probabilistic framework. First, the relay–RTU–SCADA event chain is verified through controlled current-injection testing in a 35 kV reserve feeder bay. Second, residual earth-fault current along the 9.4 km Prizreni 1–Zhuri overhead feeder is evaluated using IEC 60909 single-phase-to-earth simulations implemented in DIgSILENT PowerFactory. Probabilistic threshold-exceedance analysis is then applied to estimate detection reliability as a function of feeder distance. The simulated residual current decreases from 350.577 A near the source substation to 299.793 A at the feeder endpoint. For the deployed 300 A pickup threshold,

© 2026. The Author(s). This is an open-access article distributed under the terms of the Creative Commons Attribution-NonCommercial-NoDerivatives License (CC BY-NC-ND 4.0, https://creativecommons.org/licenses/by-nc-nd/4.0/), which permits use, distribution, and reproduction in any medium, provided that the Article is properly cited, the use is non-commercial, and no modifications or adaptations are made.

the detection probability decreases from near-unity values in upstream feeder sections to approximately 0.49 at the remote end of the feeder. Additional sensitivity analysis shows that fault resistance, uncertainty level, pickup threshold, and feeder electrical length significantly influence practical detectability limits. The results demonstrate that residual earth-fault indication in long feeders should be evaluated as a probabilistic distance-dependent problem rather than as a purely deterministic threshold-crossing condition. The presented framework provides an engineering basis for evaluating reliability limits and pickup-threshold adequacy in medium-voltage distribution.

Key words: detection reliability, IEC 60909, medium-voltage feeder, Monte Carlo simulation, probabilistic assessment, residual current, residual earth-fault indicator

1. Introduction

Reliable earth-fault detection is a fundamental operational requirement in medium-voltage distribution feeders. In long radial overhead lines, the residual current component $3I_0$ decreases with increasing electrical distance from the source due to cumulative line impedance and grounding conditions [1]. Consequently, the residual current available for fault indication varies along the feeder [2, 3].

Fault passage indicators installed in distribution networks operate with fixed pickup thresholds [4]. Under such settings, the difference between the residual fault current and the pickup threshold varies with feeder location [5, 6]. Near the substation, this margin is typically sufficient to ensure stable operation. In remote feeder sections, however, the margin may approach the configured threshold, making indicator response sensitive to variations in fault resistance, grounding conditions, and network modelling assumptions [7, 8].

This limitation becomes particularly relevant in practical monitoring architectures, where fault detection relies on SCADA supervision combined with selectively installed line indicators [9–12]. Although various fault-location methods have been reported, including impedance-based, signal-processing, and data-driven approaches [13, 14], many require measurement density and communication infrastructure that are not available in typical overhead distribution feeders [15, 16]. In such conditions, fault monitoring continues to depend on supervisory observation and distributed fault passage indicators rather than dense synchronized measurement systems [17–19].

Within this framework, two distinct technical conditions govern the reliability of fault indication. The first is the correct transmission of protection events through the relay−RTU−SCADA chain, which determines whether events are registered at the supervisory level [20–22]. The second is the electrical detectability of the fault at the indicator location, determined by the relationship between residual current magnitude and the configured pickup threshold [23, 24]. These conditions are operationally linked but physically different and should not be evaluated as a single problem.

Most published evaluations of fault passage indicators are based on deterministic short-circuit calculations derived from steady-state fault analysis [13, 22, 25]. In this formulation, indicator operation is treated as a binary outcome defined by the nominal residual current at the point of interest. This representation becomes inadequate when the available residual-current margin is small, as the detection outcome then depends on uncertainty in fault resistance, grounding conditions, and modelling assumptions [2, 23]. The literature provides limited quantitative analysis of how fixed-threshold indicator behaviour changes along the feeder as the available operating margin approaches the pickup threshold [26–28]. The research gap is therefore not the absence of fault-current calculation, but the absence of a distance-dependent reliability characterization of indicator detectability under practical feeder conditions.

This study addresses the identified gap using a 9.4 km, 35 kV overhead feeder as a practical case study. Residual earth-fault indication is evaluated as a location-dependent probabilistic problem rather than a nominal pass/fail condition. The analysis separates event-transmission integrity from electrical detectability. The protection–RTU–SCADA acquisition chain is verified experimentally through controlled current-injection testing [20], while residual current levels along the feeder are obtained from IEC 60909 single-phase-to-earth simulations implemented in DIgSILENT PowerFactory [29]. Indicator behaviour is then evaluated using Monte Carlo-based stochastic modelling to quantify detectability as the residual-current margin approaches the pickup threshold [30].

The contribution of the work is threefold. First, supervisory event-chain validation and electrical fault detectability are treated as distinct evaluation domains. Second, the probability of indicator operation is quantified as a function of feeder position and residual-current margin under fixed pickup settings. Third, critical detection regions and reliability limits are identified, including the behaviour associated with a 300 A pickup threshold in the analysed feeder. The presented framework combines supervisory event-chain verification, feeder-level short-circuit modelling, and probabilistic threshold-exceedance analysis in order to identify reliability limits associated with fixed-threshold earth-fault indicators. Additional feeder-length scenarios are considered to evaluate the influence of electrical length on practical detectability under the same pickup setting. The obtained results provide a distance-dependent assessment of indicator operation under practical medium-voltage feeder conditions.

2. Materials and methods

The methodological framework used in this study evaluates fault passage indicator performance in the investigated 35 kV distribution feeder at two distinct but operationally connected levels: supervisory event transmission through the protection–RTU–SCADA chain and electrical detectability of single-phase-to-earth faults at the indicator location [20, 31]. The analysed network is operated by the Kosovo Electricity Distribution Company and includes voltage levels of 35 kV, 20 kV, 10 kV, and 6 kV. The analysis focuses on the 35 kV overhead feeder connecting the Prizreni 1 and Zhuri substations. The feeder has a total length of 9.4 km and is constructed with Al–Ce 70 mm^2 conductor. The investigated feeder corridor together with the location of the installed fault passage indicators is shown in Fig. 1.

Fig. 1. Investigated 35 kV Prizreni 1–Zhuri overhead feeder corridor and installed fault passage indicator locations [32, 33]

The feeder was modelled in DIgSILENT PowerFactory using the network topology, line configuration, and operating structure of the investigated 35 kV corridor. The implemented network model together with the adopted line-parameter configuration are presented in Fig. 2, while the technical parameters used in the short-circuit study are summarized in Table 1.

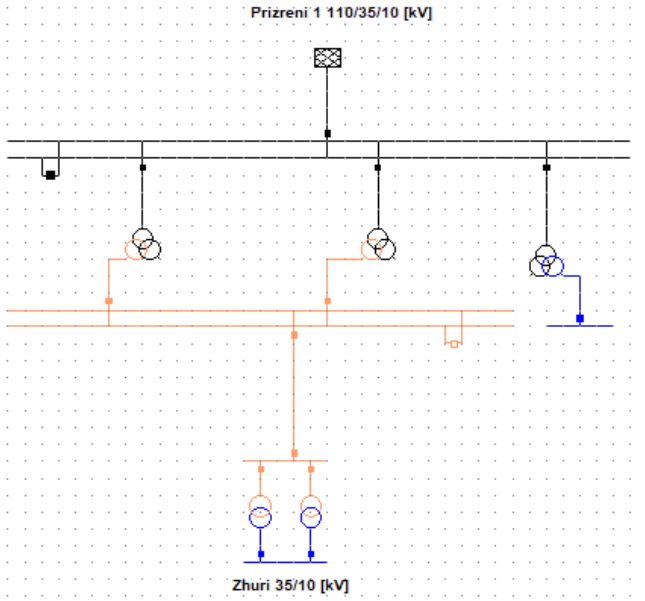

Fig. 2. PowerFactory implementation of the investigated 35 kV feeder: network model [32, 33]

Table 1. Technical parameters of the Prizreni 1–Zhuri 35 kV overhead feeder used in simulations [32, 33]

Parameter	Value
Line type	Overhead line model based on PowerFactory library parameters
Nominal voltage	35 kV
Conductor type	Al-Ce 70 mm^2
Feeder length	9.4 km
Rated current	0.235 kA
Positive-sequence resistance (R_1)	4.16 Ω
Positive-sequence reactance (X_1)	4.01 Ω
Positive-sequence impedance (Z_1)	5.78 Ω
Positive-sequence impedance angle	43.95°
Zero-sequence resistance (R_0)	12.45 Ω

Table continued on the next page

Table continued from the previous page

Parameter	Value
Zero-sequence reactance (X_0)	12.04 Ω
Source short-circuit current at 35 kV busbar	8.80 kA
Source short-circuit power	533.31 MVA
Earth factor magnitude	0.667
Short-circuit calculation standard	IEC 60909
Operating condition for fault study	Normal network topology (all sources in service)
Treatment of load during fault simulations	Loads included
35 kV neutral grounding at source substation	Isolated neutral configuration confirmed by utility operator (KEDS)
Fault impedance in simulations (R_f)	Base-case simulations performed under solid-fault assumption ($R_f = 0$ Ω). Additional sensitivity analysis was performed for resistive fault conditions.

The line parameters used in the feeder model correspond to the existing utility configuration and were confirmed by the utility operator during the revision process.

Protection functions at the substations are implemented by numerical relays interfaced with remote terminal units, allowing protection-originated events to be transmitted to the supervisory control and data acquisition system through a fiber-optic communication path. The installed fault passage indicator operates with non-directional logic, a residual-current pickup threshold of 300 A, and an intentional delay of 150 ms. The monitored activation quantity is the residual current magnitude $3I_0$. Since reliable fault indication depends both on correct event transmission and on sufficient electrical pickup margin, these two aspects were evaluated separately in order to distinguish supervisory-event transmission from physical earth-fault detectability.

Experimental validation was first carried out to verify the integrity of the protection–RTU–SCADA event chain. The tests were performed at a reserve 35 kV feeder bay in the Lipjani substation equipped with 300/5 A current transformers and a numerical relay. The configuration of the test setup, including protection parameters, communication path, and time-synchronization condition, is reported in Table 2. Controlled current injection was performed using an Omicron CMC test set with Test Universe software. Balanced three-phase currents were injected simultaneously into phases L1, L2, and L3 to trigger relay pickup and event transmission under deterministic overcurrent conditions while suppressing residual-current components. The experimental procedure therefore evaluates the integrity of the relay–RTU–SCADA communication chain, but not the physical zero-sequence sensing behaviour of the installed fault passage indicator under actual earth-fault conditions.

The applied current levels, namely 360 A, 390 A, and 420 A, corresponding respectively to 1.2, 1.3, and 1.4 times the 300 A pickup reference, are summarized in Table 3. The injected currents, relay response, and corresponding SCADA event registration are presented in Fig. 3. Each injection level was repeated ten times. No missing event, incorrect feeder identification, or inconsistent timestamping was observed during the repeated tests. SCADA event latency was not measured and is therefore outside the scope of the present study.

Table 2. Configuration and parameters used for SCADA protection signal transmission testing at the 35 kV Lipjani substation feeder bay [32, 33]

Parameter	Value
Substation	Lipjani
Feeder bay	Reserve 35 kV feeder
Protection relay	Numerical relay
Protection function	Overcurrent protection (ANSI 50/51) used to trigger relay events for SCADA-chain validation
CT ratio	300/5 A
Pickup reference	300 A (1.0 pu)
Test equipment	Omicron CMC
Test software	Test Universe
Test repetition	$N = 10$ repetitions per injection level
SCADA time synchronization	NTP
SCADA event latency	Not measured
Communication path	Relay → RTU → fiber-optic link → SCADA

Table 3. Injected current levels used during relay validation testing [32, 33]

Parameter	Value
Injection method	Balanced three-phase injection (L1, L2, L3)
Injected current – Case 1	360 A (1.2 × pickup reference)
Injected current – Case 2	390 A (1.3 × pickup reference)
Injected current – Case 3	420 A (1.4 × pickup reference)
Repetitions per case	$N = 10$

The electrical detectability analysis was carried out in DIgSILENT PowerFactory using IEC 60909 single-phase-to-earth short-circuit calculations. The simulation model includes the Prizreni 1 and Zhuri substations, the associated 35 kV overhead feeder, line sections, buses, and connected network elements under normal operating topology with all sources in service. Loads were retained in the model in order to preserve consistency with the adopted feeder representation. The computational setup used for the earth-fault study is shown in Fig. 4 [29, 34].

Single-phase-to-earth faults were simulated at ten discrete positions corresponding to 10%, 20%, . . . , 100% of the total feeder length, yielding distances from 0.94 km to 9.40 km measured from the sending-end substation. For each location, the residual current magnitude $3I_0$ was extracted from the PowerFactory short-circuit result set at the monitored feeder location used for indicator pickup assessment. These values constitute the nominal residual-current profile used for deterministic and probabilistic detectability evaluation. The simulated steady-state earth-fault current values for the ten analysed fault locations are reported in Table 4.

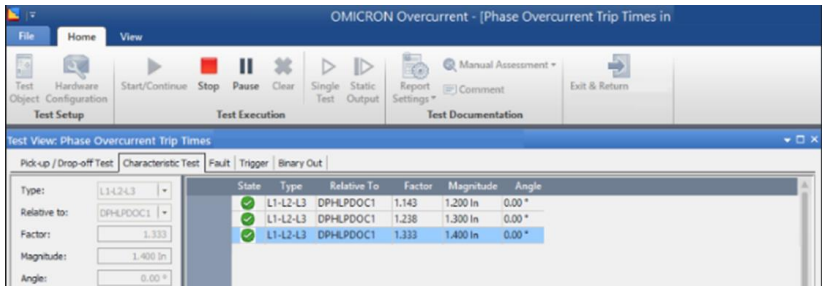

(a)

RTU Date/Time	System Date/Time	B1	B2	B3	Element	Description	Status
		LIPJANI		H12			
02/11/2022 12:56:21.608	02/11/2022 12:56:21.734	LIPJANI	35 kV	H12-REZERVE	GENERAL TRIP		
02/11/2022 12:56:21.608	02/11/2022 12:56:21.737	LIPJANI	35 kV	H12-REZERVE	RELAY PICK UP		app
02/11/2022 12:56:21.608	02/11/2022 12:56:21.737	LIPJANI	35 kV	H12-REZERVE	67-1/1 TRIP		
02/11/2022 12:56:21.758	02/11/2022 12:56:21.834	LIPJANI	35 kV	H12-REZERVE	RELAY PICK UP		disp

(b)

Fig. 3. Experimental verification of the relay–RTU–SCADA event chain: (a) omicron overcurrent injection test configuration; (b) corresponding SCADA event registration [32, 33]

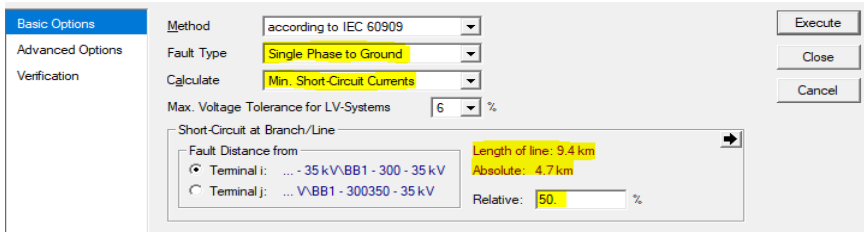

Fig. 4. PowerFactory setup used for single-phase-to-earth fault simulation at a selected feeder location [32, 33]

Table 4. Simulated steady-state earth-fault current values for ten fault locations

Simulation	Relative %	Distance [km]	Residual current $3I_0$ [A]
1	10	0.94	350.577
2	20	1.88	344.098
3	30	2.82	337.855
4	40	3.76	331.834
5	50	4.70	326.025
6	60	5.64	320.416
7	70	6.58	314.997
8	80	7.52	309.760
9	90	8.46	304.695
10	100	9.40	299.793

Additional clarification regarding network grounding and modelling assumptions was obtained from the utility operator during the revision process. The investigated 35 kV feeder operates under an isolated-neutral configuration at the source substation. The feeder model was implemented using IEC 60909 single-phase-to-earth short-circuit calculations under normal operating topology with all sources in service. The adopted line parameters, conductor configuration, and feeder length were confirmed by the utility operator and correspond to the actual investigated feeder section. Detailed modelling of grounding-impedance variation and Petersen-coil behaviour was outside the scope of the present study.

The base-case fault simulations were performed using a solid-fault assumption ($R_f = 0\ \Omega$), which is commonly adopted in short-circuit studies to evaluate the maximum available earth-fault current and the corresponding detection margin. Since resistive earth faults may significantly influence residual-current magnitude and fault detectability, additional sensitivity analysis under resistive-fault conditions was incorporated during the revision process in order to examine the influence of fault resistance on threshold-exceedance probability and detection reliability.

The neutral-grounding impedance itself was not explicitly represented in the available PowerFactory implementation. Consequently, the obtained residual-current values should be interpreted within the adopted zero-sequence network representation and IEC 60909 modelling assumptions. The analysis therefore focuses on detectability trends, operating margins, and threshold sensitivity along the feeder under the adopted modelling assumptions.

To examine the influence of electrical length beyond the investigated 9.4 km feeder, additional feeder-length scenarios of 6 km, 12 km, and 18 km were also considered. These scenarios constitute a parametric extension of the base feeder model and are used to examine the sensitivity of detectability to electrical length under the same modelling assumptions. They are not intended to reproduce fully reconstructed independent feeder configurations.

For each simulated fault location at distance d, the deterministic pickup margin relative to the installed indicator threshold was defined as:

$$M(d) = I_{\mathrm{res}}(d) - I_{\mathrm{th}}, \tag{1}$$

where $I_{\mathrm{res}}(d)$ is the simulated residual earth-fault current magnitude $3I_0$ at distance d, and $I_{\mathrm{th}} = 300$ A is the configured pickup threshold. Positive values of $M(d)$ indicate nominal threshold exceedance, whereas negative values indicate that the nominal residual current is below the pickup setting. This quantity represents the deterministic residual-current headroom available at each feeder position.

Because the residual current may vary with modelling uncertainty, grounding conditions, and operating assumptions, the robustness of fixed-threshold pickup was further evaluated through a probabilistic model. At each location, the residual current was represented as a Gaussian random variable centred at the nominal simulated value [27, 35]:

$$I_{\mathrm{res}}(d) = \mu(d) + \varepsilon, \tag{2}$$

$$\varepsilon \sim N\left(0, \sigma^2(d)\right), \tag{3}$$

$$\sigma(d) = 0.04\,\mu(d), \tag{4}$$

where $\mu(d)$ is the nominal residual current obtained from the PowerFactory simulation. The 4% dispersion level was adopted as a moderate engineering uncertainty assumption intended to

represent the combined influence of current-transformer accuracy, relay pickup tolerance, fault passage indicator measurement uncertainty, modelling approximations, and operational variability under practical feeder conditions. The adopted uncertainty level is additionally consistent with the combined measurement tolerances reported for the installed current transformers, relay protection functions, and fault passage indicator measurement chain by the utility operator. The Gaussian representation is therefore treated as an engineering approximation intended for probabilistic sensitivity analysis rather than as a strict statistical characterization of residual-current behaviour under all operating conditions.

The probability of indicator pickup at distance d was then defined as:

$$P_{\mathrm{det}}(d) = P\left(I_{\mathrm{res}}(d) > I_{\mathrm{th}}\right). \tag{5}$$

Under the Gaussian assumption defined in (2)–(4), the probability of threshold exceedance can also be expressed analytically as:

$$P_{\mathrm{det}}(d) = 1 - \Phi\left(\frac{I_{\mathrm{th}} - \mu(d)}{\sigma(d)}\right), \tag{6}$$

where $\Phi(\cdot)$ denotes the cumulative distribution function of the standard normal distribution. This expression gives the probability that the residual current exceeds the pickup threshold under the adopted uncertainty model.

Monte Carlo simulation with 20 000 trials was performed for each fault location, and the detection probability was estimated as the fraction of realizations satisfying $\widetilde{I}_{\mathrm{res}}(d) > I_{\mathrm{th}}$. For the investigated feeder conditions, 20 000 trials per location were sufficient to obtain numerically stable probability estimates. Where reliability-distance limits are reported later in continuous form, they are obtained by interpolation between adjacent simulated points rather than by direct reading from the ten discrete simulation locations. Discrete fault-location results and interpolated reliability-distance limits are therefore reported separately in the Results section in order to avoid ambiguity in interpretation.

3. Results

The monitoring framework was evaluated at two distinct levels. First, the integrity of protection-event acquisition within the relay–RTU–SCADA chain was experimentally verified. Second, feeder-level electrical detectability of single-phase-to-earth faults was quantified using IEC 60909 short-circuit simulations and uncertainty-aware post-processing. The separation between these evaluation levels is necessary because correct SCADA-event transmission does not by itself guarantee reliable residual-current pickup at the installed fault passage indicator location.

The SCADA-chain verification confirmed that protection-originated events were registered correctly under deterministic overcurrent conditions substantially above threshold. No missed event, incorrect feeder identification, or inconsistent timestamping was observed during the repeated tests. The performed balanced three-phase injection therefore validates the relay−RTU−SCADA communication path, whereas earth-fault detectability remains dependent on residual-current magnitude, fault resistance, grounding configuration, and the pickup setting of the installed fault passage indicator.

The feeder-level analysis examines whether the deployed 300 A residual-current pickup provides adequate detectability over the full 9.4 km feeder length. The simulated steady-state residual-current values are summarized in Table 4 and illustrated in Fig. 5. The residual current decreases monotonically from 350.577 A at 0.94 km to 299.793 A at 9.40 km, corresponding to an absolute attenuation of 50.784 A, or 14.5% relative to the upstream value. Over the final 4 km of the feeder, the current decreases from 326.025 A to 299.793 A, confirming progressive reduction of pickup headroom in the distal feeder section. As the residual current approaches the configured pickup threshold, the operating margin becomes increasingly sensitive to uncertainty and threshold variation.

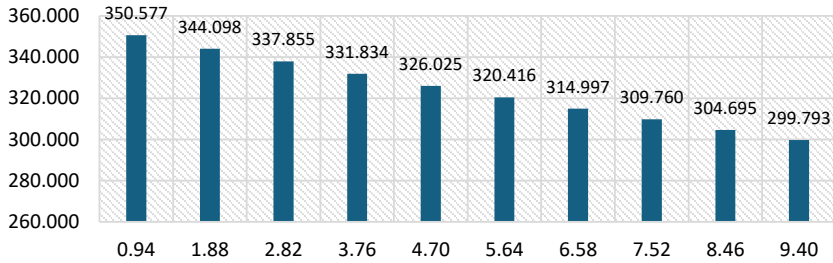

Fig. 5. Variation of steady-state earth-fault current along the feeder as a function of fault distance [32, 33]

At the installed indicator location of 4.70 km, the simulated residual current is 326.025 A, corresponding to a deterministic pickup margin of 26.025 A, or 8.7% above the 300 A threshold. At 8.46 km, the margin decreases to 4.695 A, while at 9.40 km it reaches −0.207 A. The operating point therefore transitions from clear threshold exceedance in the upstream and mid-feeder sections toward a near-threshold condition at the remote end of the feeder. Under such conditions, deterministic threshold exceedance alone is insufficient for evaluating practical pickup reliability. The uncertainty-bounded residual-current envelope is presented in Fig. 6, the corresponding pickup-margin profile is shown in Fig. 7, and the associated numerical results are summarized in Table 5.

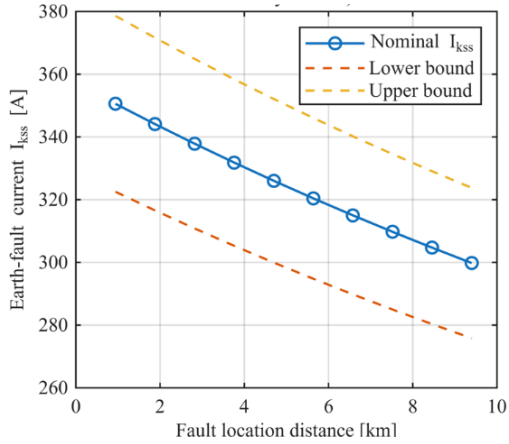

Fig. 6. Residual earth-fault current profile along the feeder with associated uncertainty bounds

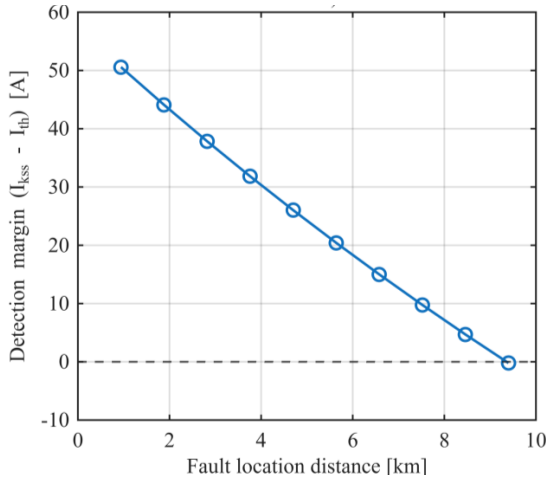

Fig. 7. Detection margin as a function of fault distance along the feeder

Table 5. Summary of fault distance, residual current, detection margin, and probability of detection

Simulation	Distance [km]	Residual current $3I_0$ [A]	Margin M [A]	Detection probability P_{det}
1	0.94	350.577	50.577	0.99985
2	1.88	344.098	44.098	0.99980
3	2.82	337.855	37.855	0.99675
4	3.76	331.834	31.834	0.99090
5	4.70	326.025	26.025	0.97750
6	5.64	320.416	20.416	0.94380
7	6.58	314.997	14.997	0.88190
8	7.52	309.760	9.760	0.78715
9	8.46	304.695	4.695	0.64955
10	9.40	299.793	–0.207	0.48965

The residual-current uncertainty envelope shown in Fig. 6 confirms that the available pickup margin decreases progressively with increasing feeder distance. In the upstream feeder region, the uncertainty bounds remain clearly above the pickup threshold, indicating stable operating conditions with sufficient deterministic headroom. Toward the remote feeder sections, the uncertainty interval approaches and eventually intersects the threshold region, indicating increased sensitivity of indicator operation to relatively small residual-current variations.

The pickup margin decreases approximately linearly from about 50 A near the sending end to zero near the feeder endpoint. When the margin falls below approximately 10 A, corresponding to the 7.5–8 km region, the indicator enters a low-headroom operating regime in which relatively small residual-current variations become operationally significant. In the final feeder section, where the deterministic margin remains within approximately ±5 A of the threshold, the pickup decision becomes highly sensitive to uncertainty. This behaviour is reflected in the probability-of-detection

profile shown in Fig. 8. The values summarized in Table 5 show that the probability of detection decreases from 0.99985 at 0.94 km to 0.97750 at the installed location, then to 0.64955 at 8.46 km, and finally to 0.48965 at the feeder endpoint. The obtained results indicate a gradual transition from deterministic threshold exceedance toward uncertainty-dominated probabilistic operation as feeder distance increases.

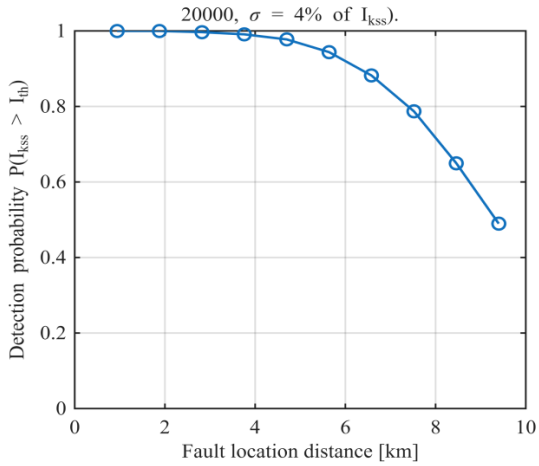

Fig. 8. Probability of fault detection as a function of fault distance obtained from Monte Carlo simulation

A field event reported by the utility operator was additionally used for consistency checking of the simulated residual-current profile. The operational event data obtained from SCADA records are summarized in Table 6, while the comparison between measured and simulated residual-current values is presented in Fig. 9.

Table 6. Operational earth-fault event used for consistency checking

Parameter	**Value**
Event date	09 January 2025
Event times	17:55 and 18:43–18:44
Feeder	F-ZHURI
Voltage level	35 kV
Approximate fault location	7.43 km
Measured residual current	306 A
Simulated residual current near same section	309.760 A at 7.52 km
Difference	approximately 3.760 A
Initial event	TRIP/momentary fault
Later event	TRIP/permanent fault
SCADA registration	Fault detect events registered

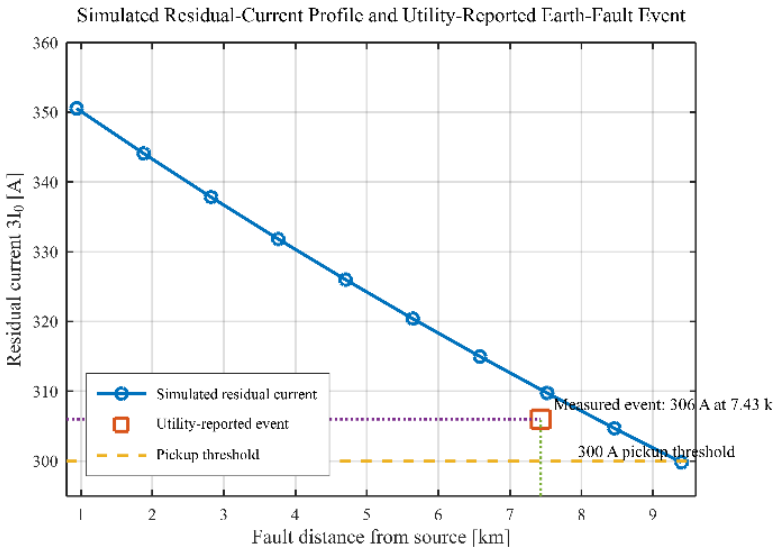

Fig. 9. Simulated residual-current profile together with utility-reported earth-fault event location and measured residual current

The reported event was registered at an approximate distance of 7.43 km with a measured residual current of 306 A. The corresponding simulated value near the same feeder section equals 309.760 A at 7.52 km, resulting in a deviation of approximately 3.760 A, or about 1.2%. Considering the uncertainties associated with fault-location estimation, measurement accuracy, and operational conditions, the obtained agreement is satisfactory for practical feeder-level analysis. The agreement supports the engineering consistency of the adopted feeder model.

The recorded event is located close to the operating region where the residual current approaches the configured pickup threshold of the fault passage indicator. Under such conditions, relatively small current variations may influence threshold exceedance and indicator operation. The operational event therefore supports the probabilistic detectability behaviour identified in the previous analysis, particularly in the remote feeder sections where the available pickup margin becomes limited. The SCADA event sequence additionally confirms the expected operating behaviour of the installed non-directional fault passage indicator during momentary and permanent earth-fault conditions.

The effect of pickup-threshold selection is examined in Fig. 10, which shows current margin as a function of feeder distance for pickup settings of 280 A, 290 A, 300 A, and 310 A. The corresponding detection probabilities are presented in Fig. 11. The results show that relatively small threshold adjustments produce substantial changes in effective detection coverage along the feeder. For the deployed 300 A threshold, operation remains highly reliable at the indicator location, but reliability decreases rapidly once the deterministic margin collapses in the distal feeder section. Lowering the threshold to 290 A preserves positive nominal headroom across almost the full feeder, whereas increasing the threshold to 310 A shifts the zero-margin intersection upstream.

Under the adopted uncertainty model, the effect is nonlinear. Reducing the mean margin from approximately 26 A to about 5 A decreases the detection probability from about 0.98 to about 0.65. At the feeder endpoint, where the nominal operating point approaches the configured threshold,

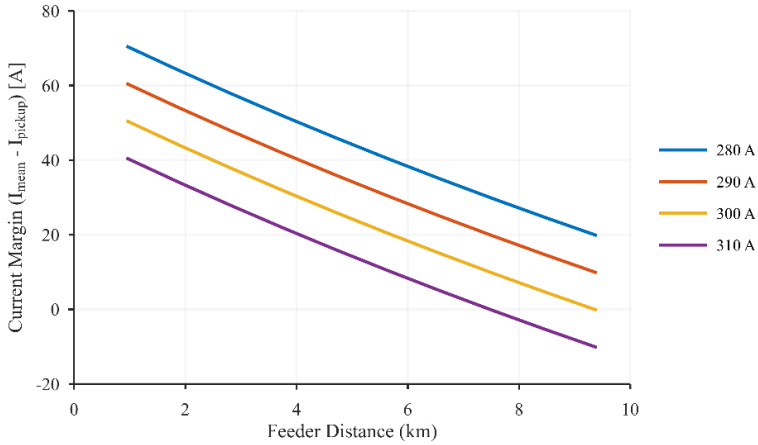

Fig. 10. Current margin versus feeder distance for multiple pickup thresholds

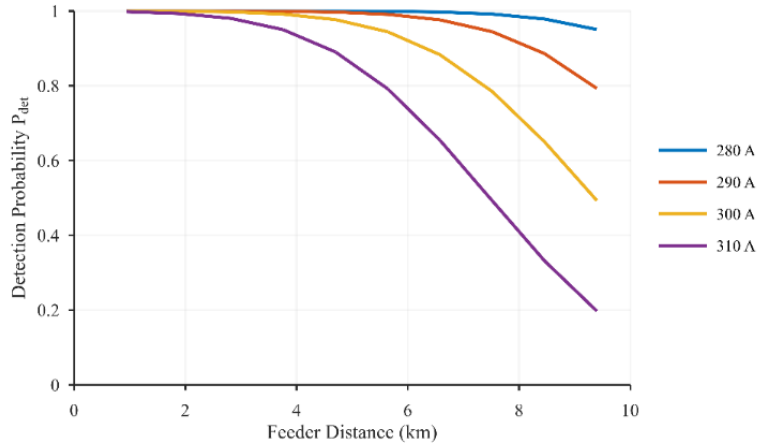

Fig. 11. Detection probability versus feeder distance for different pickup thresholds

the probability of detection decreases to approximately 0.49. The obtained behaviour confirms that the transition from deterministic to probabilistic operation develops progressively as the residual-current margin approaches the pickup threshold of the installed indicator.

The influence of uncertainty magnitude is isolated in Fig. 12, where the same nominal residual-current profile is evaluated using dispersion levels of 2%, 4%, 6%, and 8%. In upstream sections, where deterministic headroom remains large, the probability of detection is weakly affected by uncertainty. In contrast, once the mean operating point approaches the threshold, dispersion becomes the controlling factor. Under the adopted model, increasing uncertainty broadens the transition region and accelerates the decline in distal-end reliability. The effect becomes most pronounced in the low-margin operating region beyond approximately 7 km, where relatively small variations in residual current significantly affect threshold exceedance probability. This behaviour is characteristic of threshold-based devices operating near their decision boundary.

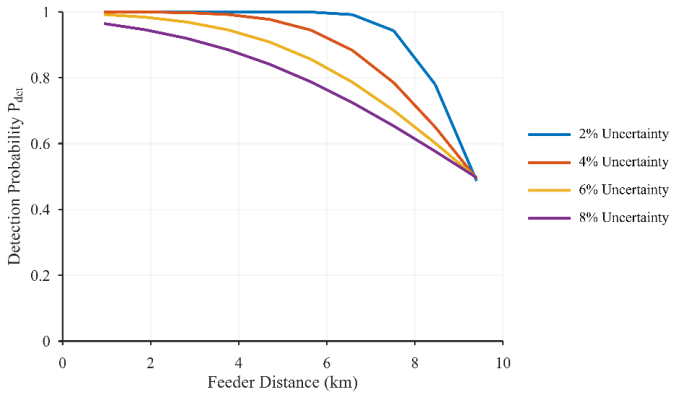

Fig. 12. Detection probability sensitivity to uncertainty level

In addition to pickup-threshold and uncertainty sensitivity, the revised analysis includes the influence of fault resistance. This addition was introduced because resistive earth faults can significantly reduce residual-current magnitude and therefore change the probability that a fixed-threshold indicator will operate. The fault-resistance cases are treated as a parametric sensitivity extension based on the existing residual-current profile and are not presented as additional PowerFactory recalculations. The base case corresponds to $R_f = 0\ \Omega$, while additional resistive-fault conditions are evaluated for $R_f = 10\ \Omega$, $R_f = 50\ \Omega$, and $R_f = 100\ \Omega$.

The results presented in Table 7 show that the residual-current magnitude decreases significantly with increasing fault resistance. Under the solid-fault condition $R_f = 0\ \Omega$, the simulated residual current remains close to the 300 A pickup threshold along the entire feeder length, decreasing from 350.58 A near the source side to 299.79 A at the remote end of the feeder. When resistive-fault conditions are introduced, the residual-current profile changes substantially. For $R_f = 10\ \Omega$, the residual current decreases below the 300 A pickup threshold along the entire feeder, including locations close to the source substation. Additional increases in fault resistance produce a further reduction of residual-current magnitude. For $R_f = 50\ \Omega$ and $R_f = 100\ \Omega$, the calculated residual-current values remain considerably below the pickup setting throughout the investigated corridor. The obtained results show that practical detectability is governed by the combined influence of feeder attenuation, pickup threshold, and fault resistance rather than by feeder distance alone. The obtained trends should be interpreted together with the isolated-neutral grounding configuration adopted for the investigated 35 kV feeder, since grounding practice directly influences residual-current magnitude during single-phase-to-earth faults.

Figure 13 illustrates the corresponding detection-probability profiles obtained for different fault-resistance conditions.

Under the solid-fault assumption $R_f = 0\ \Omega$, the detection probability remains close to unity over a large portion of the feeder and decreases progressively toward the remote end, where the residual current approaches the pickup threshold. For $R_f = 10\ \Omega$, the probability of detection decreases sharply even at short feeder distances, confirming that relatively small increases in fault resistance may significantly affect indicator operation. Under $R_f = 50\ \Omega$ and $R_f = 100\ \Omega$, the predicted detection probability approaches zero across the entire feeder length because the residual-current magnitude remains substantially below the adopted pickup setting.

Table 7. Fault-resistance sensitivity of residual-current detectability

Distance [km]	Residual current $3I_0$ at $R_f = 0\ \Omega$ [A]	Residual current $3I_0$ at $R_f = 10\ \Omega$ [A]	Residual current $3I_0$ at $R_f = 50\ \Omega$ [A]	Residual current $3I_0$ at $R_f = 100\ \Omega$ [A]
0.94	350.58	298.75	187.73	128.19
1.88	344.10	294.03	185.86	127.31
2.82	337.86	289.46	184.02	126.45
3.76	331.83	285.03	182.22	125.59
4.70	326.03	280.73	180.45	124.75
5.64	320.42	276.56	178.72	123.92
6.58	315.00	272.52	177.02	123.10
7.52	309.76	268.59	175.36	122.29
8.46	304.70	264.77	173.72	121.50
9.40	299.79	261.06	172.12	120.71

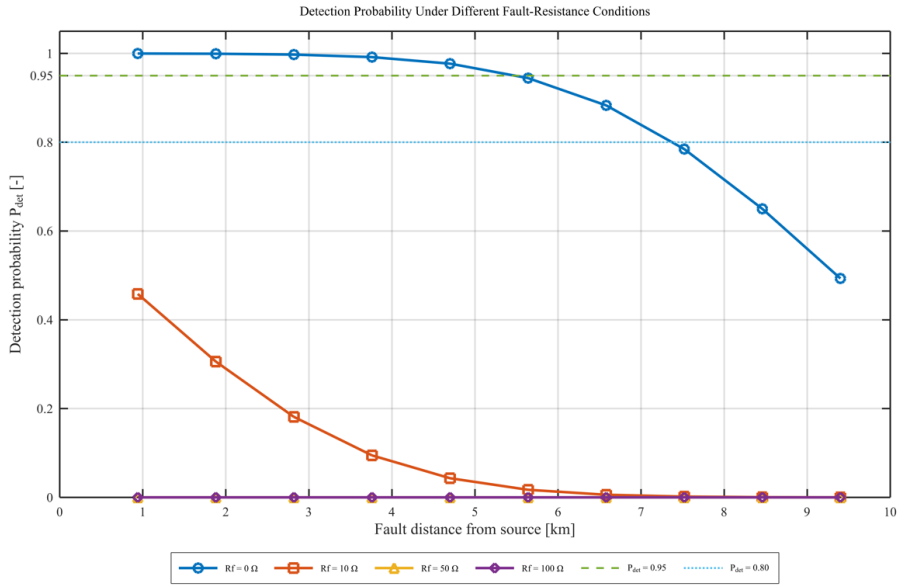

Fig. 13. Detection probability along the feeder under different fault-resistance conditions

The reliability-distance limits summarized in Table 8 quantify the operational consequences of increasing fault resistance. For the solid-fault condition $R_f = 0\ \Omega$, the deterministic detection limit extends to approximately 9.36 km, while the high-reliability operating regions are reduced to 5.48 km for $P_{\text{det}} \geq 0.95$ and 7.37 km for $P_{\text{det}} \geq 0.80$. Once resistive-fault conditions are introduced, these operational limits collapse rapidly. For $R_f = 10\ \Omega$, the calculated probabilities

remain below the adopted reliability criteria over the entire feeder length, resulting in zero reliability-distance coverage according to the selected thresholds. The same behaviour is observed for $R_f = 50\ \Omega$ and $R_f = 100\ \Omega$, where the predicted detection probability becomes negligible. The analysis therefore confirms that resistive-fault behaviour must be considered when evaluating practical FPI deployment limits in medium-voltage feeders.

Table 8. Reliability-distance limits under different fault-resistance conditions

Fault resistance R_f [Ω]	**MaxDist $M \geq 0$ [km]**	**MaxDist $P_{\text{det}} \geq 0.95$ [km]**	**MaxDist $P_{\text{det}} \geq 0.80$ [km]**	P_{min}	P_{avg}
0	9.36	5.48	7.37	0.493	0.872
10	0.00	0.00	0.00	0.0001	0.111
50	0.00	0.00	0.00	0.0000	0.000
100	0.00	0.00	0.00	0.0000	0.000

The influence of feeder electrical length is further examined through parametric feeder-length scenarios. The investigated 9.4 km feeder was used as the reference case (Table 9),and three additional scenarios were considered for 6 km, 12 km, and 18 km using the same pickup threshold and the same modelling assumptions. The deterministic margin trajectories are shown in Fig. 14, and the corresponding detection probabilities as a function of normalized distance are shown in Fig. 15. The compact feeder maintains positive headroom over nearly its full length, whereas the long-feeder scenario approaches the pickup boundary as feeder electrical length increases. As feeder electrical length increases, the available residual-current margin decreases progressively, causing the probability-of-detection transition region to shift toward shorter normalized distances.

Table 9. Reliability distance limits as a function of pickup threshold

Pickup threshold [A]	**Max. distance $M \geq 0$ [km]**	**Max. distance $P_{det} \geq 0.95$ [km]**	**Max. distance $P_{det} \geq 0.80$ [km]**	P_{min}	P_{max} / P_{avg}
280	9.4	9.4	9.4	0.95059	1 / 0.99172
290	9.4	7.3607	9.3287	0.79293	0.99999 / 0.95872
300	9.3603	5.4789	7.3726	0.49311	0.99984 / 0.87205
310	7.4769	3.7602	5.5619	0.19734	0.9981 / 0.72795

To further support the practical relevance of the feeder-length sensitivity analysis, additional utility-provided data were reviewed for another 35 kV overhead corridor with a total length of approximately 21 km and Al/Ce 95/15 conductor configuration. The feeder operates within the same regional network environment and exhibits line parameters of $R_1 = 6.72\ \Omega$, $X_1 = 8.23\ \Omega$, $R_0 = 20.16\ \Omega$, and $X_0 = 24.69\ \Omega$. The reviewed utility data additionally confirm the presence of long 35 kV overhead feeders within the same operating network.

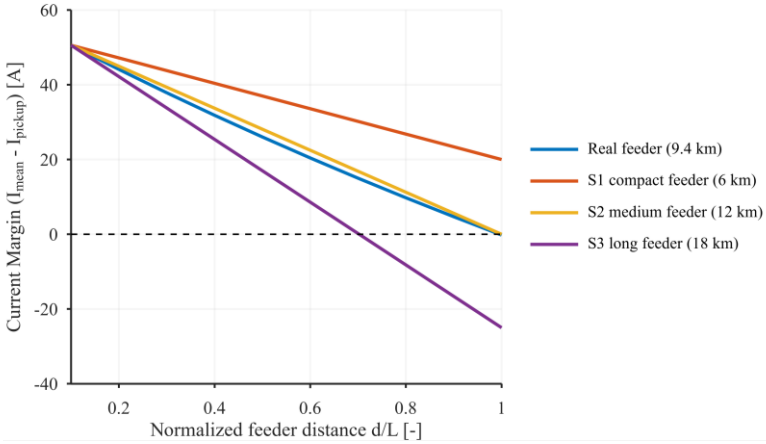

Fig. 14. Detection margin as a function of normalized feeder distance for representative feeder scenarios

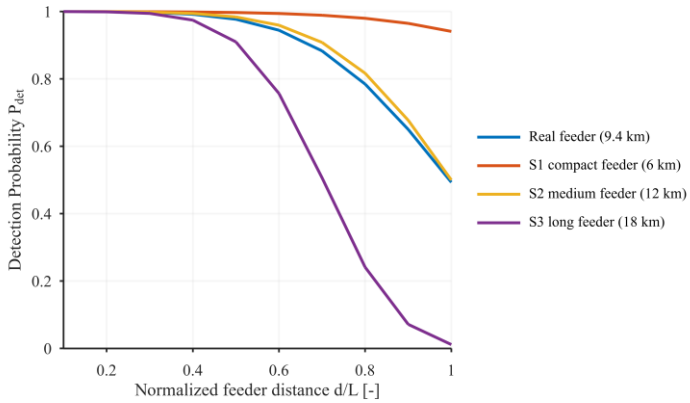

Fig. 15. Detection probability versus normalized feeder distance for representative feeder scenarios

The reliability metrics for the representative feeder-length scenarios are summarized in Table 10. Under the common 300 A pickup threshold, the compact feeder maintains high detectability over nearly its full length, whereas the medium and long-feeder scenarios exhibit a progressive reduction in reliable coverage. For the investigated 9.4 km feeder, the interpolated reliability limits are 9.3603 km for nonnegative deterministic margin, 5.4789 km for a detection probability of at least 0.95, and 7.3726 km for a detection probability of at least 0.80.

The long-feeder scenario exhibits the strongest degradation of detectability performance. In the 18 km case, the minimum probability of detection decreases to 0.012, indicating that substantial portions of the feeder operate close to or below the adopted pickup threshold.

The combined results show that feeder distance, pickup threshold, uncertainty level, and fault resistance jointly determine practical detectability limits of fixed-threshold FPIs. Under the adopted modelling assumptions, the deployed 300 A threshold remains operationally acceptable at the present indicator location but does not provide uniformly high reliability over the full feeder

Table 10. Reliability limits across representative feeder scenarios for a 300 A pickup threshold

Feeder	**Length [km]**	**MaxDist $M \geq 0$ [km]**	**MaxDist $P \geq 0.95$ [km]**	**MaxDist $P \geq 0.80$ [km]**	$P_{\min}$	$P_{\max}$	P_{avg}
Real feeder, Prizreni 1–Zhuri (9.4 km)	9.4	9.3603	5.4789	7.3726	0.493	1	0.872
S1 compact feeder (6 km)	6	6	5.4	6	0.941	1	0.986
S2 medium feeder (12 km)	12	12	7.2	9.6	0.5	1	0.884
S3 long feeder (18 km)	18	12.6	7.2	9	0.012	1	0.646

length. The most critical operating region corresponds to the distal feeder sections, where the residual current approaches the pickup threshold and relatively small variations in operating conditions may influence indicator operation.

4. Conclusions

The performed analysis shows that the detectability of single-phase-to-earth faults in the investigated 35 kV feeder is governed by the available residual-current margin relative to the configured pickup threshold of the fault passage indicator. IEC 60909 simulations indicate that the residual current decreases from 350.577 A near the sending-end substation to 299.793 A at the feeder endpoint, corresponding to an attenuation of approximately 14.5% along the 9.4 km feeder. As the residual-current margin approaches the pickup threshold, fault indication progressively shifts from deterministic operation toward uncertainty-sensitive probabilistic behaviour.

For the deployed 300 A pickup threshold, the installed indicator location at 4.70 km maintains satisfactory operating margin and a detection probability of approximately 0.98. In contrast, the distal feeder sections operate close to the pickup boundary, where the detection probability decreases to approximately 0.49. The results additionally show that relatively small threshold variations significantly influence practical monitoring coverage and reliability-distance limits.

The additional fault-resistance analysis demonstrated that resistive-fault conditions substantially reduce residual-current magnitude and detection probability under fixed-threshold operation. Under increased fault resistance, the residual current decreases below the pickup setting over large portions of the feeder, resulting in rapid degradation of practical detectability. The comparative feeder-length analysis further confirmed that long feeders operate with substantially reduced reliability margins under the same pickup threshold.

Experimental current-injection tests verified correct relay-event transmission through the relay–RTU–SCADA communication chain, while comparison with a utility-reported earth-fault event showed satisfactory agreement between simulated and measured residual-current values.

The obtained detectability limitations are therefore associated primarily with feeder electrical conditions rather than communication failure within the supervisory infrastructure.

The presented framework combines deterministic short-circuit analysis with probabilistic threshold-exceedance evaluation and sensitivity analysis of pickup threshold, uncertainty level, fault resistance, and feeder electrical length. Under the adopted modelling assumptions, the deployed 300 A pickup threshold remains operationally acceptable at the present indicator location but does not provide uniformly high reliability over the full feeder length.

Future work should include explicit modelling of grounding impedance, additional field-based calibration of uncertainty parameters, and evaluation of adaptive pickup strategies for improving earth-fault detectability in medium-voltage distribution feeders.

Acknowledgements

The authors acknowledge the Kosovo Electricity Distribution Company (KEDS) for providing access to internal technical reports and operational data used in this study.

References

[1] Hamatwi E., Imoru O., Kanime M.M., Kanelombe H.S.A., *Comparative Analysis of High Impedance Fault Detection Techniques on Distribution Networks*, IEEE Access, vol. 11, pp. 25817–25834 (2023), DOI: 10.1109/ACCESS.2023.3254923.

[2] Achitaev A.A., Suslov K.V., Volkova I.O., Kozhemyakin V.E., Dvoryansky Y.V., *Development of an algorithm for identifying single-phase ground fault conditions in cable and overhead lines in the networks with isolated neutral*, Energy Reports, vol. 9, pp. 1079–1086 (2023), DOI: 10.1016/j.egyr.2023.01.046.

[3] Bindi M., Piccirilli M.C., Luchetta A., Grasso F., *A Comprehensive Review of Fault Diagnosis and Prognosis Techniques in High Voltage and Medium Voltage Electrical Power Lines*, Energies, vol. 16, no. 21, 7317 (2023), DOI: 10.3390/en16217317.

[4] Yang Z., Xie C., Yin C., *Fault Location Method for Distribution Network Using an Additional Inductance Strategy*, Electronics, vol. 13, no. 4, 712 (2024), DOI: 10.3390/electronics13040712.

[5] Quintero J.J.V., De Araújo J.V.G., Faria W.R., Pereira Junior B.R., *Fault indicator placement in distribution systems: Improving the criteria of quality of service*, Electric Power Systems Research, vol. 234, 110761 (2024), DOI: 10.1016/j.epsr.2024.110761.

[6] Rasoulnia M., Yaghoubi E., Yaghoubi E., Hussain A., Kamwa I., *A comprehensive systematic and bibliometric review of technologies and measurement tools for power quality events detection, classification, and fault location in smart grids*, Renewable and Sustainable Energy Reviews, vol. 226, 116302 (2026), DOI: 10.1016/j.rser.2025.116302.

[7] Medattil Ibrahim A.H., Sharma M., Subramaniam Rajkumar V., *Integrated Fault Detection, Classification and Section Identification (I-FDCSI) Method for Real Distribution Networks Using μPMUs*, Energies, vol. 16, no. 11, 4262 (2023), DOI: 10.3390/en16114262.

[8] Pattanaik V. *et al.*, *A critical review on phasor measurement units installation planning and application in smart grid environment*, Results in Engineering, vol. 24, 103559 (2024), DOI: 10.1016/j.rineng.2024.103559.

[9] Caballero-Peña J., Cadena-Zarate C., Parrado-Duque A., Osma-Pinto G., *Distributed energy resources on distribution networks: A systematic review of modelling, simulation, metrics, and impacts*, International Journal of Electrical Power & Energy Systems, vol. 138, 107900 (2022), DOI: 10.1016/j.ijepes.2021.107900.

[10] Sakai R.T. *et al.*, *Architecture Deployment for Application of Advanced Distribution Automation Functionalities in Smart Grids*, J Control Autom. Electr. Syst., vol. 33, no. 1, pp. 219–228 (2022), DOI: 10.1007/s40313-021-00799-6.

[11] Mnyanghwalo D.C., Kawambwa S.J., *Sensor placement algorithm for faults detection in electrical secondary distribution network using dynamic programming method: focusing on dynamic change and expansion of the network configurations*, Journal of Electrical Systems and Inf. Technol., vol. 11, no. 1, 13 (2024), DOI: 10.1186/s43067-024-00135-3.

[12] Sun G. *et al.*, *A Fault Location Method for Medium Voltage Distribution Network Based on Ground Fault Transfer Device*, Electronics, vol. 12, no. 23, 4790 (2023), DOI: 10.3390/electronics12234790.

[13] Cavalari C.F., Martins A.S.C., Penido D.R.R., Araujo L.R.D., *An enhanced method for fault location in distribution systems based on optimal power flow*, International Journal of Electrical Power & Energy Systems, vol. 157, 109870 (2024), DOI: 10.1016/j.ijepes.2024.109870.

[14] Chen K., Hu J., Zhang Y., Yu Z., He J., *Fault Location in Power Distribution Systems via Deep Graph Convolutional Networks*, IEEE J. Select. Areas Commun., vol. 38, no. 1, pp. 119–131 (2020), DOI: 10.1109/JSAC.2019.2951964.

[15] Ding C. *et al.*, *Research on feeder automation-assisted fault diagnosis method based on distribution network fault indication system*, IET Conf. Proc., vol. 2025, no. 26, pp. 12–16 (2025), DOI: 10.1049/icp.2025.3154.

[16] Li H., Wu Y., Chen M., *Adaptive Fault-Tolerant Tracking Control for Discrete-Time Multiagent Systems via Reinforcement Learning Algorithm*, IEEE Trans. Cybern., vol. 51, no. 3, pp. 1163–1174 (2021), DOI: 10.1109/TCYB.2020.2982168.

[17] Conte F., D'Agostino F., Gabriele B., Schiapparelli G.-P., Silvestro F., *Fault Detection and Localization in Active Distribution Networks Using Optimally Placed Phasor Measurements Units*, IEEE Trans. Power Syst., vol. 38, no. 1, pp. 714–727 (2023), DOI: 10.1109/TPWRS.2022.3165685.

[18] Quintero J.J.V., De Araújo J.V.G., Faria W.R., Pereira Junior B.R., *Fault indicator placement in distribution systems: Improving the criteria of quality of service*, Electric Power Systems Research, vol. 234, 110761 (2024), DOI: 10.1016/j.epsr.2024.110761.

[19] Zhang D., Zhang W., Wang C., Xiao X., *Fault Segment Location for MV Distribution System Based on the Characteristic Voltage of LV Side*, Electronics, vol. 12, no. 7, 1734 (2023), DOI: 10.3390/electronics12071734.

[20] Aghahadi M., Bosisio A., Merlo M., Berizzi A., Pegoiani A., Forciniti S., *Digitalization Processes in Distribution Grids: A Comprehensive Review of Strategies and Challenges*, Applied Sciences, vol. 14, no. 11, 4528 (2024), DOI: 10.3390/app14114528.

[21] Majeed Butt O., Zulqarnain M., Majeed Butt T., *Recent advancement in smart grid technology: Future prospects in the electrical power network*, Ain Shams Engineering Journal, vol. 12, no. 1, pp. 687–695 (2021), DOI: 10.1016/j.asej.2020.05.004.

[22] Khan S., Aboushady A.A., Ul Nazir F., Farrag M.E., *Fault Detection and Localization in LV Distribution Networks Using Anomaly Detection in Smart Meter Data and Distribution Network Digital Twin*, IEEE Access, vol. 14, pp. 17525–17539 (2026), DOI: 10.1109/ACCESS.2026.3659724.

[23] Lukowicz M., *Optimized bandpass admittance criteria for earth fault identification in medium-voltage networks with isolated neutral*, International Journal of Electrical Power & Energy Systems, vol. 117, 105618 (2020), DOI: 10.1016/j.ijepes.2020.105855.

[24] Jabbar F.I. *et al.*, *Detection of single line to ground fault and self-extinguishing by using a variable and a fixedable inductance in distribution grid in power*, IJPEDS, vol. 14, no. 4, 2044 (2023), DOI: 10.11591/ijpeds.v14.i4.pp2044-2051.

[25] Abed N.K., Abed F.T., Al-Yasriy H.F., ALRikabi H.T.S., *Detection of power transmission lines faults based on voltages and currents values using K-nearest neighbors*, IJPEDS, vol. 14, no. 2, 1033 (2023), DOI: 10.11591/ijpeds.v14.i2.pp1033-1043.

[26] Yoon D.-H., Yoon J., *Development of a real-time fault detection method for electric power system via transformer-based deep learning model*, International Journal of Electrical Power & Energy Systems, vol. 159, 110069 (2024), DOI: 10.1016/j.ijepes.2024.110069.

[27] MansourLakouraj M., Hosseinpour H., Livani H., Benidris M., *Waveform Measurement Unit-Based Fault Location in Distribution Feeders via Short-Time Matrix Pencil Method and Graph Neural Network*, IEEE Trans. on Ind. Applicat., vol. 59, no. 2, pp. 2661–2670 (2023), DOI: 10.1109/TIA.2022.3231586.

[28] Buzo R.F. *et al.*, *Frequency Response Assessment of Distribution Feeders with Capacitor Banks for Voltage Harmonic Mitigation: A Practical Approach With Field Measurements*, IEEE Access, vol. 13, pp. 70616–70625 (2025), DOI: 10.1109/ACCESS.2025.3562733.

[29] Strezoski L.V., González-Longatt H.M., Katić V.A., *Quantifying the impact of inverter-based distributed energy resources modelling on IEC 60909 short-circuit calculations*, Electric Power Systems Research, vol. 224, 109638 (2023), DOI: 10.1016/j.ijepes.2023.109161.

[30] Łowczowski K., Olejnik B., *Monitoring, Detection and Locating of Transient Earth Faults in MV Networks Using Cable Screen Earthing Current Measurements*, Energies, vol. 15, no. 3, 1043 (2022), DOI: 10.3390/en15031043.

[31] Peter G., Stonier A.A., Gupta P., Gavilanes D., Vergara M.M., Lung Sin J., *Smart Fault Monitoring and Normalizing of a Power Distribution System Using IoT*, Energies, vol. 15, no. 21, 8206 (2022), DOI: 10.3390/en15218206.

[32] Kosovo Electricity Distribution Company (KEDS), *SCADA Installation and Operational Architecture Report (Internal Technical Report)*, Kosovo Electricity Distribution Company, Prishtina, Kosovo (2022).

[33] Wei M., Shi F., Zhang H., Chen W., Xu B., *Detection and Feeder Identification of the High Impedance Fault at Distribution Networks Based on Synchronous Waveform Distortions*, IEEE Transactions on Smart Grid, vol. 12, no. 1, pp. 612–623 (2021), DOI: 10.1109/TSG.2020.3016752.

[34] Deepak D., Rudion K., John C., Abele H., *Improved Accuracy in Calculation of Initial Fault Current in Converter-based Power Systems*, 2024 IEEE PES Innovative Smart Grid Technologies Europe (ISGT EUROPE), Dubrovnik, Croatia: IEEE, pp. 1–5 (2024), DOI: 10.1109/ISGTEUROPE62998.2024.10863342.

[35] Rezapour H., Jamali S., Bahmanyar A., *Review on Artificial Intelligence-Based Fault Location Methods in Power Distribution Networks*, Energies, vol. 16, no. 12, 4636 (2023), DOI: 10.3390/en16124636.